Enhanced room-temperature spin-valley coupling in V-doped MoS_2

Krishna Rani Sahoo,[1] Janmey Jay Panda,[1] Sumit Bawari,[1] Rahul Sharma,[1] Dipak Maity,[1] Ashique Lal,[1] Raul Arenal,[2,3,4] G. Rajalakshmi,[1] and Tharangattu N. Narayanan[1,*]

[1]*Tata Institute of Fundamental Research-Hyderabad, Sy. No. 36/P, Gopanapally Village, Serilingampally Mandal, Hyderabad-500046, India*

[2]*Instituto de Nanociencia y Materiales de Aragon (INMA), Universidad de Zaragoza, 50009 Zaragoza, Spain*

[3]*Laboratorio de Microscopias Avanzadas (LMA), Universidad de Zaragoza, 50018 Zaragoza, Spain*

[4]*Fundación ARAID, 50018 Zaragoza, Spain*

(Received 16 March 2022; revised 24 June 2022; accepted 11 August 2022; published 23 August 2022)

Achieving room-temperature valley polarization in two-dimensional (2D) atomic layers (2D materials) by substitutional doping opens new avenues of applications. Here, monolayer MoS_2, when doped with vanadium at low (0.1 atomic %) concentrations, is shown to exhibit high spin-valley coupling, and hence a high degree of valley polarization at room-temperature. The atomic layers of MoS_2 (MS) and V-doped MoS_2 (VMS) are grown via the chemical vapor deposition-assisted method. The formation of new energy states near the valence band is confirmed from band gap calculations and also from the density functional theory–based band structure analyses. Time-reversal symmetry broken energy shift in the equivalent valleys is predicted in VMS, and the room-temperature chirality-controlled photoluminescent (PL) excitation measurements indicate such a shift in valley exciton energies (∼35 meV). An enhanced valley polarization in VMS (∼42%) is observed in comparison to that in MS (<12%), while in MS, the chirality-controlled excitations did not show the difference in emission energies. Spin Hall effect of light–based optical rotation measurements indicate the asymmetric absorption among the two different chiralities of the incident light, hence supporting the existence of room-temperature valley polarization. This study opens possibilities of room-temperature opto-spintronics using stable 2D materials.

DOI: 10.1103/PhysRevMaterials.6.085202

I. INTRODUCTION

Two-dimensional transition metal dichalcogenides (TMDs) offer control over a new degree of freedom called valley for electrons (e.g., holes, excitons) apart from charge and spin [1]. This comes about due to the breaking of inversion symmetry (K↑, K′↓) in monolayers [2]. Electrons in the valence band of TMD monolayers such as MoS_2 (MS) can be excited to conduction band minima, where these energy minima have the same energy but have different crystal momenta depending on the orientation of the crystal axes [3]. These minima are called valleys and they can be selectively populated by different external fields/forces [4–6], and this population difference creates valley polarization [7–9]. Considerable momentum separation of these valleys also makes this a robust degree of freedom in TMDs for valleytronics applications [10,11]. Apart from the breaking of the inversion symmetry, time-reversal symmetry can also be broken in MS-like TMDs [6,12–14]. This allows a spin–momentum locking and the possibility of selective polarization of valleys using another external force called chirality-selected optical excitation [4,15].

The optical chirality (left or right circular polarization)-selected valley polarization is possible in MS [4]. Resonant optical excitations also limit the intervalley transition and scattering, and hence spin-selective polarization can be achieved by chirality-controlled optical excitations [15]. One of the ways to distinguish between the valleys is by an external magnetic field, and few reports have shown this [13,16,17]. A very large magnetic field, 0.1 to 0.2 meV/T, required for lifting up the valley degeneracy by breaking time-reversal symmetry limits its practical application [12,14]. Recent studies have tried to enhance valley polarization using interfacial magnetic exchange fields by making heterojunctions with a magnetic substrate or by a magnetic insulator where magnitude and sign of valley polarization can be controlled [17,18]. It has been shown theoretically that valley degeneracy can also be broken using magnetic impurity doping in TMDs using transition metals as dopants [19]. Valley imbalance is realized in the Mn-doped MoS_2 system, but the valley shift is far from the Fermi level due to charge transfer, making it impractical for applications [20]. Enhancement in valley splitting in Fe-doped MoS_2 was recently demonstrated by Li *et al.* [21] at room-temperature using a high magnetic field of ∼7 T. Another theoretical study states that permanent valley polarization can be achieved in Cr- and V-doped TMDs [19]. A recent study on V-doped WSe_2 shows room-temperature ferromagnetism with approximately 10% polarization [22]. As V doping creates states near to the valence band, it causes large splitting in the valence band. In chemical vapor deposition (CVD)-assisted growth of MS, it also introduces *p*-doping in otherwise *n*-type material, causing an increase in the radiative recombination process due to neutral excitons. In this study, the possibility

*tnn@tifrh.res.in

of large Zeeman splitting due to V doping in MS (VMS) is verified and the valley polarization is proved via two different techniques: chirality-selective photoluminescence (PL) and weak value amplification-aided spin Hall effect of light (SHEL) measurements. A density functional theory (DFT)–based detailed theoretical study is conducted to correlate the observed valley and spin polarizations.

The SHEL creates spatial separation between opposite chiralities of light when a polarized light beam is reflected by a surface. In SHEL-based reflection measurements, appropriate selection of polarization pointer states before and after the reflection of a Gaussian light beam enable one to enhance the signals significantly due to the interaction of light with the samples (MS and VMS) [23]. The complex optical beam shift happens due to the spin-orbit interaction of light with the material and the changes in the underlying geometric phase [23–26]. This allows the quantification of chirality-dependent absorption, and polarization rotation due to interaction with material more precisely [27,28]. Here, such a SHEL-based high-sensitivity measurements are used to study the valley polarization and resulting asymmetric absorption (in chirality) in VMS compared to that of MS.

II. EXPERIMENTAL METHODS

A. Growth of V-doped MoS_2

V-doped MoS_2 is grown over Si/SiO_2 substrate using the CVD method. A two-zone furnace is used for the growth wherein downstream (zone I) sulfur and upstream a different weight ratio (1:5 ratio) of MoO_3 and V_2O_5 powder is loaded in the alumina boat, as illustrated in Supplemental Material Fig. S1 [29]. The Si/SiO_2 substrate is placed over the mixture powder facing downward in heating zone II. The growth temperature of zone II is set to 710 °C (15 minutes) for metal decomposition, where the sulfur temperature is kept at 180 °C (15 minutes) in zone I to follow the sulfurization process. The furnace is maintained at a constant flow of N_2 (190 sccm) during the whole growth procedure. After growth, the tube is suddenly cooled to room-temperature to stop further multilayer growth. To vary the concentration of vanadium, the ratio of MoO_3 and V_2O_5 powder is optimized.

B. Characterization of the samples

Optical images, Raman spectra, and PL are acquired using a Renishaw Invia Raman spectroscope. Different optical excitation measurements are conducted with the Raman spectrometer by controlling the incident and emitted light chirality. In one such experiment, chirality-resolved emission is being detected from the samples with a linear polarization excitation. The samples are excited with a linear polarization and analyzed using a combination of a quarter-wave plate (QWP) and polarizer, as shown in the experimental setup of Supplemental Material Fig. S2 [29]. In another experiment, the sample is excited with a linear combination of vertical polarized light and a QWP to create one circular polarized light. Similarly, a linear combination of vertical polarized light, a half-wave plate, and a QWP are used for other circular polarized light. The schematic of the circularly polarized photoluminescence (CPL) setup is shown in Supplemental Material Fig. S2 [29].

The morphology and presence of vanadium are studied by scanning electron microscopy (SEM, JEOL). To identify the structural composition of the material, scanning transmission electron microscope (TEM) imaging is performed using a probe aberration-corrected Thermo Fisher Scientific Titan Low Base TEM microscope, operated at 120 keV. For TEM imaging, the material is transferred to a copper grid with porous carbon film using the Poly(methyl methacrylate) (PMMA) wet transfer method. The SHEL-based study is performed using a homemade setup with a 780 nm diode laser and with a 633 nm He-Ne laser as described in our previous work [23]. To identify the chemical composition of the material, X-ray photoelectron spectroscopy (XPS) is performed using a Kratos Axis Supra spectrometer equipped with a monochromatic Al Kα X-ray.

C. DFT calculations

The open-source simulation package SIESTA 4.0 has been used for DFT calculations. A 2×2 unit cell of MS is considered and a single vanadium is doped in VMS. In doping, one molybdenum atom is replaced by one vanadium atom. This doping percentage is much higher than experimental concentrations ($\sim$0.1%), but suffice for a system in which vanadium are noninteracting. The pseudopotential files are generated with the generalized gradient approximation (GGA) exchange-correlation functional, and nonlinear relativistic core corrections are incorporated for spin-orbit interactions. The Broyden method is used for structure optimization with a $16 \times 16 \times 1$ Monkhorst–Pack k-grid. The doped structure is also relaxed via Broyden relaxation, and the optimized structures are used for the analysis. All the calculations are spin polarized and the effect of spin-orbit coupling (SOC) is considered. A GGA functional is used with spin polarization and relativistic corrections to account for SOC.

III. RESULTS AND DISCUSSION

MS and VMS are synthesized on a Si/SiO_2 (300-nm) substrate using a CVD-based method, as illustrated in Supplemental Material Fig. S1 [29]. For the MS growth, MoO_3 and sulfur powders are used as the molybdenum and sulfur precursors, the details of which are found in our previous work [30]. For V doping, V_2O_5 is chosen as the vanadium precursor. In a recent report by Zou *et al.* [31], V_2O_5 is used for low-concentration V doping due to its high melting point, while other dopants such as NH_4VO_3 and VCl_3 are used for high-concentration doping. In this work, we have optimized different atomic percentages of V doping using the same precursor (V_2O_5) with the addition of a little amount of salt (NaCl), where the salt can lower the melting point of precursors [32]. The atomic percentage of vanadium can be controlled by taking different weight ratios of V_2O_5 and MoO_3. The optical and SEM images of pristine MS and VMS are shown in Supplemental Material Fig. S3 [29]. The typical lateral size of VMS is around $\sim$150 μm, as shown in Supplemental Material Fig. S3 [29]. In Supplemental Material Fig. S3(c) and (d) [29], the SEM image shows the structure of

MS and VMS, and the triangular-shaped crystal formation is evident. SEM–energy-dispersive X-ray (EDX) spectroscopy confirms the presence of molybdenum, sulfur, and vanadium elements in VMS (Supplemental Material Fig. S4 [29]).

Pristine MS has two characteristic Raman modes at 384 cm^{-1} (E_{2g}) and 404 cm^{-1} (A_{1g}) separated by ∼20 cm^{-1}, as shown in Fig. 1(a) [33]. In VMS, along with these two MS characteristic peaks, a few new Raman active modes evolve at 158 cm^{-1}, 183 cm^{-1}, 224 cm^{-1}, 324 cm^{-1}, and 350 cm^{-1} [purple and yellow regions in Fig. 1(a)] [33,34]. The position of the E_{2g} peak in VMS is found to be redshifted while the position of A_{1g} is not affected. By increasing the electron concentration in *n*-doped MS systems, electron–phonon scattering increases, as has been shown in previous reports [23], and it results in a redshift in the A_{1g} mode due to an increase in *n* carrier concentration. The *p* doping due to vanadium incorporation does not affect this A_{1g} mode in VMS. Raman modes in the purple region in Fig. 1(a) correspond to peaks evolved due to lattice symmetry breaking in the MS system after incorporation of a foreign atom (vanadium). The new peak at 324 cm^{-1} (highlighted in yellow) can be assigned to a new mode that arises due to the vanadium atom doped in the MS lattice and is sensitive to doping concentration [31].

MS exhibits intense PL centered at ∼1.89 eV upon excitation using a 532 nm laser (details in the previous section), corresponding to its optical band gap. PL measurements are conducted on both MS and VMS to investigate the changes in the optical properties due to the V doping [Fig. 1(b)]. PL intensity decreases compared to pristine monolayer MS, and a redshift is also noticed because of a decrease in optical band gap [as shown in the inset of Fig. 1(b)] [33]. The reduction in intensity corresponds to an increasing rate of more nonradiative recombination centers. To investigate further, PL spectra are deconvoluted into three peaks [neutral exciton (A^0), trion (Tr^-), and B-exciton (B)]. The ratio between Tr^- and A^0 is more in MS than VMS, as shown in Supplemental Material Fig. S5 [29], indicating a decrease in *n*-type carriers. Further increasing the vanadium dopant concentrations, PL spectra are quenched, suggesting a semiconductor-to-metallic transition of the MS lattice (Supplemental Material Fig. S6 [29]) [35]. The PL spectra are taken on low-doped VMS, ∼0.1 atomic % [calculated using XPS, discussed later; data shown in Fig. 1(b)], and it is found that the PL is completely quenched in heavily doped VMS, ∼3.7 atomic % (from XPS, data not shown), as illustrated in Supplemental Material Fig. S6 [29].

The atomic arrangements in VMS are probed using high-angle annular dark-field scanning transmission electron microscopy (HAADF-STEM)–based imaging [Fig. 1(c)]. The HAADF-STEM image of MS as reported in previous work [30] has only hexagonal sites with molybdenum as the bright circle. The formation of 1H phase VMS, with molybdenum as bright circles, while sulfur as dark is shown in Fig. 1(c). It is similar to that in MS [30], but in VMS, some molybdenum sites (molybdenum columns) are lighter in contrast to the otherwise uniform molybdenum contrast in MS, and it can be assigned to vanadium atoms as the contrast in HAADF-STEM is directly related to atomic number [36–39]. From the image analysis (the blue circles indicate the possible vanadium places in molybdenum sites), it is clear that the vanadium is well distributed in the MS lattice, replacing molybdenum in its sites. As shown in Fig. 1(d), three positions are marked, and their corresponding contrast intensity profile is plotted, confirming incorporation of vanadium in the molybdenum lattice.

XPS is carried out to study the chemical composition of the doped vanadium states, shown in Figs. 1(e)–1(g). In fact, XPS is a surface-sensitive (1–10-nm sampling depth), nondestructive analytical technique offering detection limits close to 0.01 atomic % [40]. Figures 1(e)–1(g) confirms the presence of vanadium along with molybdenum and sulfur. Figure 1(e) displays two molybdenum *3d* doublets at 230 eV, 233.3 eV, 229 eV, and 232.3 eV, along with molybdenum oxidation and sulfur 2*s* peaks at 236 eV and 227 eV, respectively. Similarly, additional peaks along with the sulfur 2*p* doublet are also observed at lower binding energies (162 eV and 163.1 eV). Splitting in molybdenum and sulfur orbitals corresponds to the incorporation of vanadium atoms because it changes the electronic environment around molybdenum and sulfur [31]. A tiny amount of vanadium is also detected (∼0.1 atomic %), as illustrated in Fig. 1(g), because the percentage of vanadium is much less than molybdenum and sulfur. XPS results confirm the V doping in the MoS_2 system.

Chirality-controlled (excitation) PL experiments are conducted on MS and VMS monolayers with an excitation energy of 2.33 eV (wavelength, 532 nm). The emissions from different valleys (K and K′), following transition rules, are polarized and they can be controlled by chirality-controlled optical excitation experiments [4]. The σ^+ polarized light will create excitons in the K valley and σ^- in K′, by following the optical transition rules [4], and observed spectra result from an energy difference in the valleys, if any. The details of the experiment are given in previous section and Supplemental Material Fig. S2 [29]. Initially, the MS and VMS samples are excited with linear polarization, and chirality-resolved PL spectra (σ^+ in magenta and σ^- in olive) emissions are collected using a combination of a quarter-wave plate and polarizer in the reflected path. In another experiment, the MS is excited with a circularly polarized light (σ^+, magenta color) of wavelength 532 nm, and then the emission spectrum is recorded. Sequentially, circularly polarized light having opposite chirality (σ^-, olive color) is used to excite MS, and the PL signal is collected. Figure 2(a) shows the polarization-resolved PL in the emission for MS under linear excitation. Figure 2(b) represents the polarization-resolved PL under chirality-controlled excitations. The position of the A-excitonic peak seems to be the same for both the chiralities in the MS sample (in both the experiments). The position and contour of the two spectra for MS are similar at room-temperature. The population of the two valleys of MS is energetically degenerate as there exists time-reversal symmetry in monolayer limits; hence, emission from both the valleys (K and K′) will be at the same energies. This is explicit from Fig. 2(a). In addition, in the next set of experiments, after being excited with different polarized (chirality) excitations (instead of linear excitation, as before), the position of their emissions is unchanged [Fig. 2(b)], confirming no intrinsic valley splitting in the MS system. Similar polarization experiments on VMS are conducted at room-temperature, and an energy shift in the emission for two different chirality excitations is observed, as

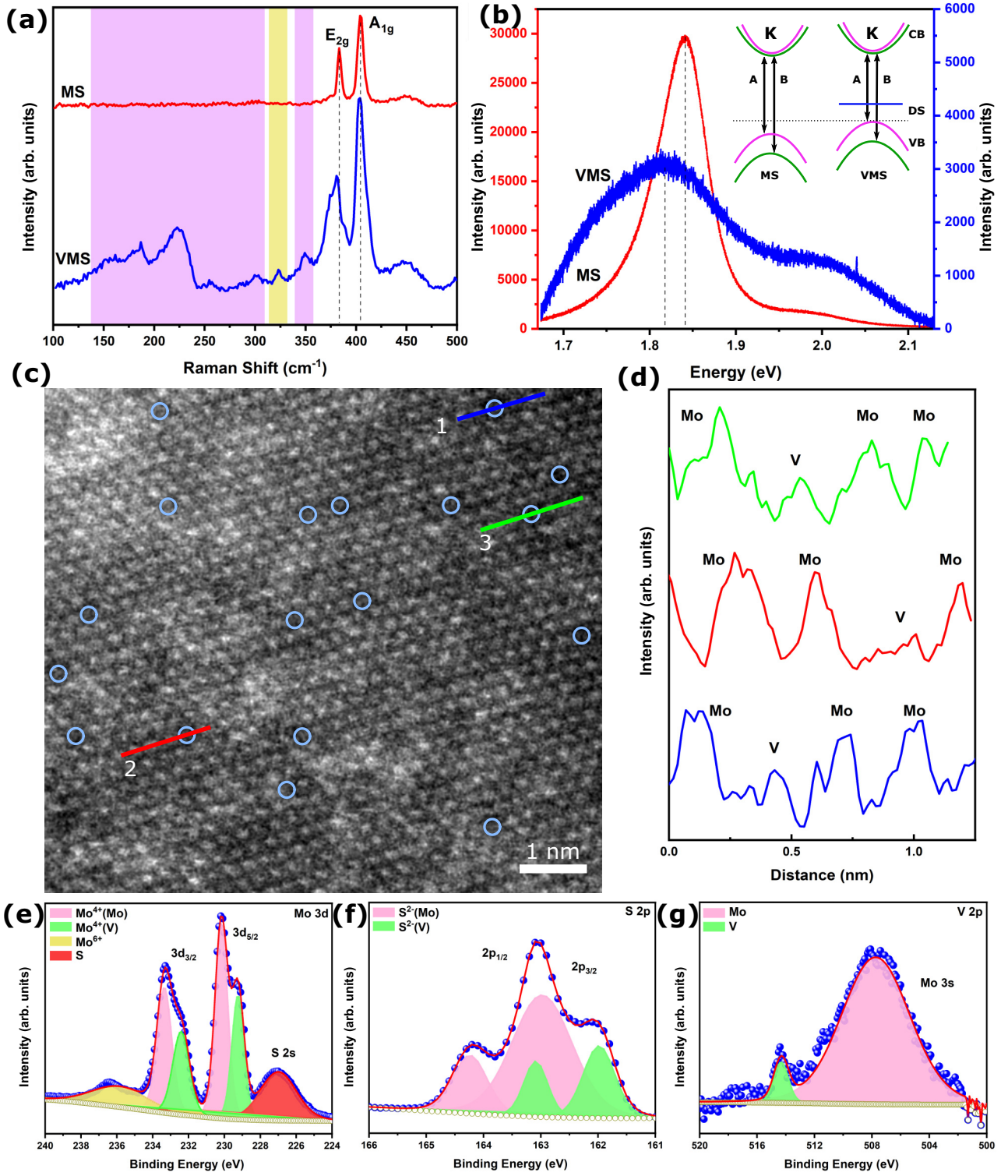

FIG. 1. Structure and morphology study. (a) Raman spectra of VMS and MS using a laser excitation of 532 nm. The highlighted portions illustrate new modes of MS. (b) PL spectra of MS and VMS at an excitation wavelength of 532 nm. The excitation is by linear vanadium polarization, and PL detection is not chirality resolved. The inset represents a possible band structure after V doping, which is further verified in the later part using XPS. Here, DS indicates the doped states, which are vanadium states created due to doping. (c) Atomic structure of V-doped MS from STEM (HAADF-STEM) showing a hexagonal lattice structure where vanadium replaces molybdenum in some random places. Vanadium sites are highlighted with blue circles. (d) The intensity line profile at three places indicates the presence of vanadium in the MS lattice. The different-colored line profiles indicate the area (color code) mentioned in (c). Chemical information from XPS analysis: XPS spectra of (e) molybdenum 3*d* orbital, (f) sulfur 2*p* orbital, and (g) vanadium 2*p* along with the molybdenum 3*s* orbital. New bonding states are observed in molybdenum and sulfur due to V doping.

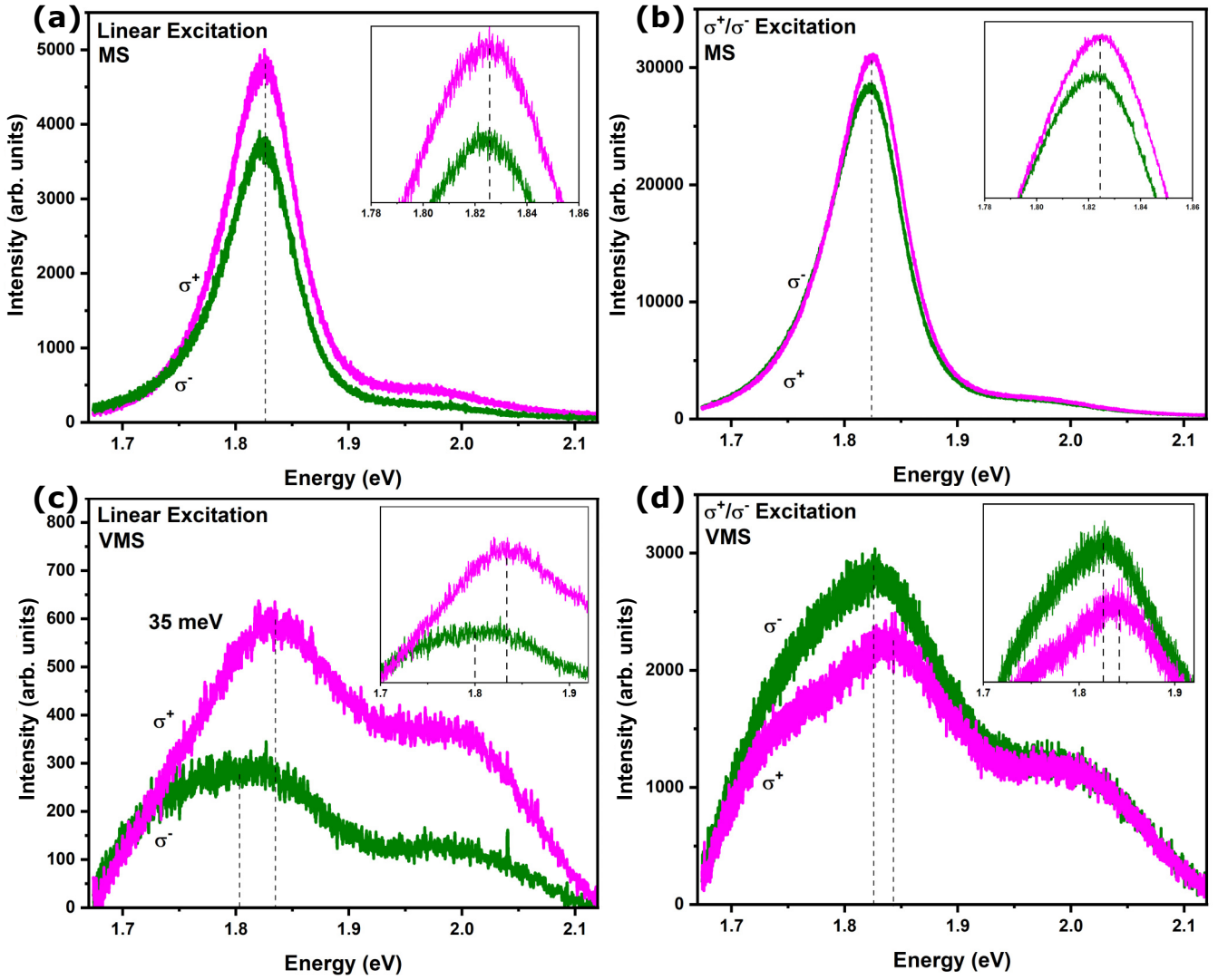

FIG. 2. PL experiments with different optical excitations ($\lambda = 532$ nm): (a) PL spectra under linear excitation and extracting two different polarizations [chirality, right (σ^+) and left (σ^-) circular] in emission for MS at room-temperature, (b) PL spectra of two different chirality excitations in MS at room-temperature, (c) PL spectra under linear excitation and extracting two different polarizations [right (σ^+) and left (σ^-) circular] in emission for VMS at room-temperature depicting valley polarization introducing ~35 meV valley splitting, and (d) PL spectra of two different chirality excitations in VMS at room-temperature show a clear valley splitting.

shown in Figs. 2(c) and 2(d). This difference is clearly seen as a shift in the PL peak position: ~35 meV between emission peaks of different chirality under linear excitations. Hence, as discussed earlier, the observed difference in the peak positions of the spectra is due to the difference in the valley energy positions. A similar shift in the valley is also observed by exciting the sample with circularly polarized light having opposite chirality. In order to confirm that the emission PL spectra of the A exciton (to ensure the emitted light's polarization is the same as the excitation) is purely circular, a polarizer is introduced in the detector path. The PL plots are taken at different analyzer angles, with the plots shown in Supplemental Material Fig. S7 [29]. The similar intensity of the observed A-excitonic peak for different analyzer angles confirms the circular nature of emitted light for both the MS and VMS samples. The degree of polarization, ($\rho = [I(\sigma^+) - I(\sigma^-)/I(\sigma^+) + I(\sigma^-)]$), is calculated and found to be ~12% for MS and ~42% for VMS at room-temperature. A small extend of room-temperature valley polarization in MS can be due to the presence of defects in the system or due the substrate effects, where it demands a detailed investigation [15,41,42]. We have performed a defect-dependent polarized PL study on MS, as shown in Supplemental Material Fig. S8 [29]. It clearly indicates that valley polarization can be manipulated by varying defects in CVD-grown pristine MS, where the defects are introduced by plasma oxidation and also by annealing in an Ar/H_2 atmosphere at 300 °C. However, a huge enhancement in valley polarization along with the difference in their peak position in VMS points toward breaking of the time-reversal symmetry at two valleys, K and K′, resulting in a change in band gap at one valley with respect to the other. Symmetry at the valleys is broken by V doping, acting as a local magnetic moment in the lattice, resulting in asymmetry in valley splitting.

To look further into the chirality-selective interaction of light with VMS, weak value amplification-based SHEL measurements are conducted. Details of the experiment can

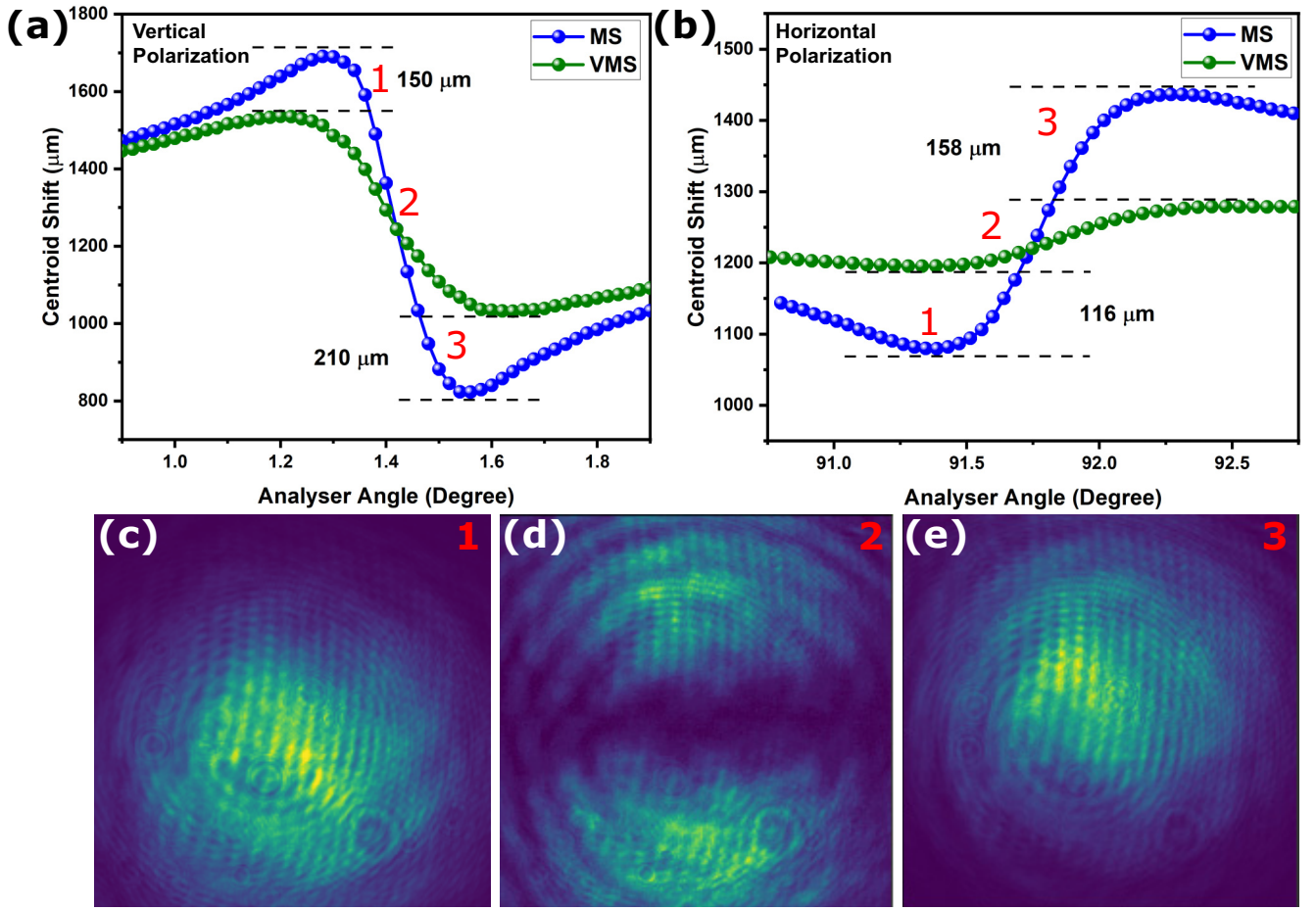

FIG. 3. The SHEL-based valley polarization study. SHEL data comparison of MS and VMS in two different initial linear polarization directions: (a) vertical (V) and (b) horizontal (H). In both configurations, the difference between σ^{+}_{MS} and σ^{+}_{VMS} is lower than that of σ^{-}_{MS} and σ^{-}_{VMS}. A 633 nm laser is used for the experiment. Typical intensity profile of SHEL shift with respect to analyzer angle from (a). (c) The maximum intensity of σ^{+} at position 1; (d) equal intensity at the center at position 2 showing the separation of two components of linear polarized light, i.e., σ^{+} and σ^{-}; and (e) the maximum intensity of σ^{-} light at position 3. A similar intensity profile is also observed for (b), which is not shown here.

be found in the previous section and Supplemental Materials Fig. S9, [29], and also in our previous work [23,26]. The experiment is performed using a Gaussian beam of horizontally or vertically polarized light in reflection geometry. The linearly polarized light is initially collimated using a lens and is incident on the sample, and light reflecting from the sample surface is observed using the weak measurements technique with a combination of analyzer in a near-orthogonal polarization state and a camera. The spatial profile of the resulting reflected light is studied with respect to analyzer angle, as shown in Fig. 3. The reflected light is observed to be spatially separated into left and right circular polarized light [Fig. 3(d)] for nearly crossed analyzer position; this phenomenon is known as the spin Hall effect of light. The separation of these two circular polarization states (vectors) (σ^{+} and σ^{-}) perpendicular to the plane of incidence can be mapped by measuring the centroid shift of the reflected beam with change in analyzer angle. Figures 3(a) and 3(b) shows the variation of the centroid with respect to the analyzer angle. The maxima and minima of the curve correspond to the beam centroid (shift) at which only one circularly polarized light is observed, as shown in Figs. 3(c) and 3(d). These experiments are performed on both MS and VMS samples. Using an initial vertically polarized light, the observed difference between the centroid position of σ^{+}_{MS} and σ^{+}_{VMS} (150 μm) is lower than that of σ^{-}_{MS} and σ^{-}_{VMS} (210 μm), as shown in Fig. 3(a). A similar experiment is carried out using horizontally polarized light, and a similar trend is noticed [Fig. 3(b)]. Apart from the difference in the centroid position of σ^{+} and σ^{-} in MS and VMS, the drastic change in slope of the SHEL curve, and the reduced shift of the circularly polarized components in VMS in comparison to that of MS signify an increase in the ellipticity of reflected light. A possible explanation for the observed behavior of the SHEL plot can be traced due to the changes introduced in the electronic band structure of MS near the Fermi level as a consequence of V doping. These changes in the electronic structure cause an unequal absorption of σ^{+} and σ^{-} polarization components, indicating an asymmetry in electronic valleys in VMS. This would lead to a difference in the reflected intensity of the two circular components, and hence the ellipticity of the reflected beam. Such a drastic change in slope and centroid shift is not observed in the case of the MS monolayer compared to the Si/SiO_2 substrate, as shown in Supplemental Material Fig. S10(a) [29], due to the

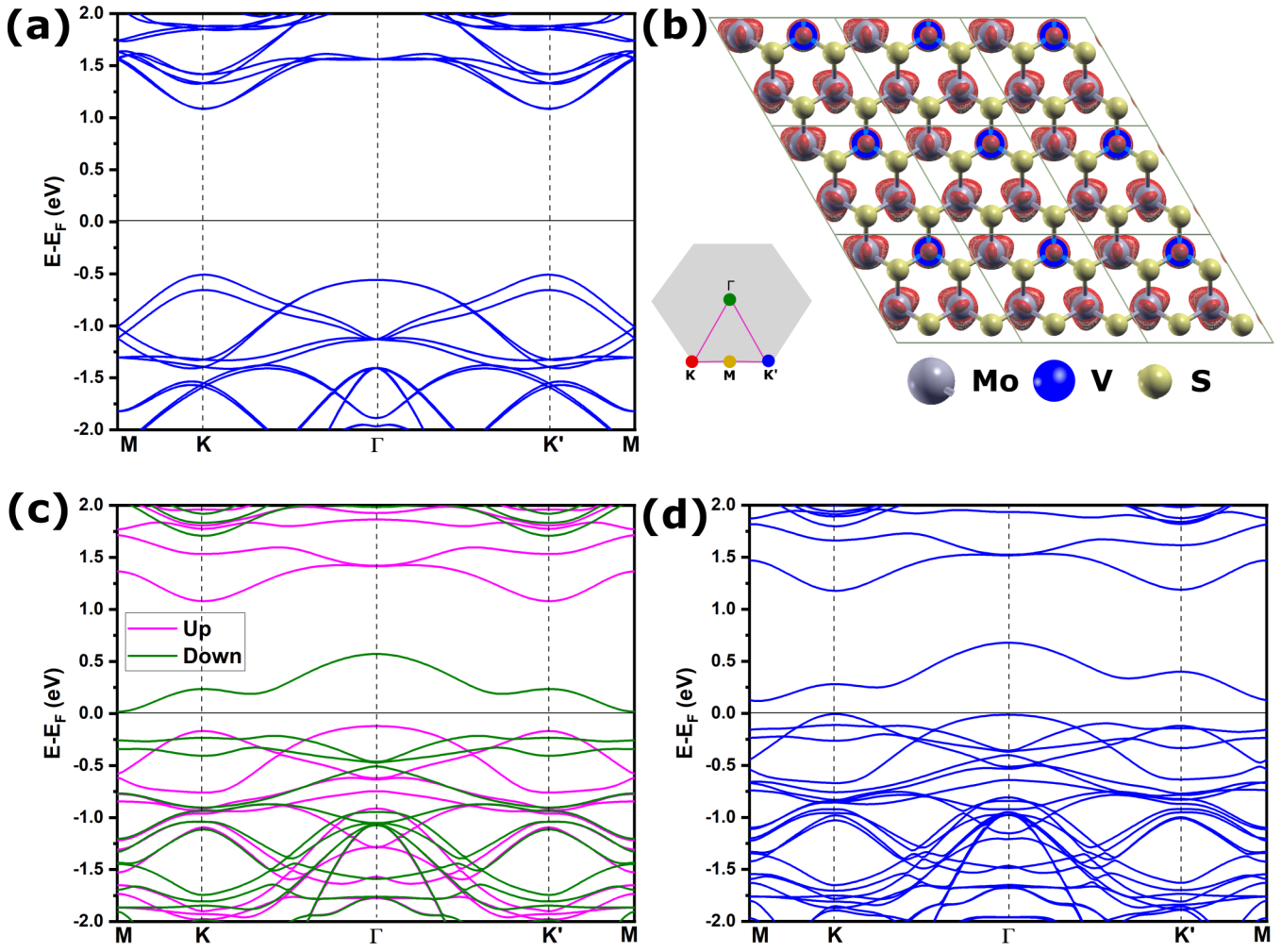

FIG. 4. Understanding the origin of valley polarization in a V-doped MS system using a DFT study. (a) Electronic band structure of pristine MS with SOC (spin-orbit coupling "on"). (b) Atomic model of a V-doped MS system with local density of states. (c) Electronic band structure of VMS without SOC (SOC "off"). Degeneracy in spin-up and spin-down at the K and K′ valleys is plotted, confirming spin polarization. (d) Electronic band diagram of VMS with SOC interaction. In all the data, the Fermi level is referred to as zero. A new state formed near the Fermi level (just above the valence band) in (d), showing a *p* doping nature. The energy difference between K and K′ is found to be 120 meV, indicating the time-reversal symmetry breaking. The SOC and spin polarization together cannot be switched on simultaneously in the DFT platform used.

absence of valley polarization. A similar experiment is carried out at 780 nm (1.58 eV), which is far below the band gap, and a similar trend is observed, as illustrated in Supplemental Material Fig. S10(b) [29]. These results provide a way to study quantitatively the asymmetry in valley dynamics of TMDs using the SHEL method.

To understand the effect of a vanadium dopant in MS, DFT-based calculations are performed. Due to SOC, as mentioned earlier, MS has a split in the valence (∼150 meV) and conduction (∼10 meV) bands that can be seen at the K and K′ symmetry points [Fig. 4(a)]. In MS, these bands exist at the same energy level while corresponding to different spin states following inversion symmetry. In a 2 × 2 MS system, one molybdenum atom is replaced with a vanadium [Fig. 4(b)] to understand the changes in properties. In these systems, paramagnetic states are induced due to the addition of vanadium atoms, and increase linearly with the addition of vanadium. To understand structure localization, the difference in energy between two vanadium atoms present as nearest neighbors and next-nearest neighbors are compared. The formation energy of the separated atoms is lower, which can explain the formation of evenly distributed vanadium atoms in MS (as seen in STEM) instead of localized domains.

With the introduction of vanadium atoms in MS, the spin splitting (without SOC) can be seen in Fig. 4(c), and by the introduction of SOC, the energy of the K and K′ valleys shift and the degeneracy is lifted. New states are formed just above the Fermi level, as shown in Supplemental Material Fig. S11 [29], which we observe as a shift of 120 meV [Fig. 4(d)] between the K and K′ symmetry points at the valence band.

The lifting of valley degeneracy is studied theoretically (∼120 meV), and experimentally verified by SHEL-based experiments and CPL-based method (∼35 meV). A deviation between the theoretical predictions and the experimental value is expected as the effect of temperature and lattice quality are not considered during calculations. The physical significance

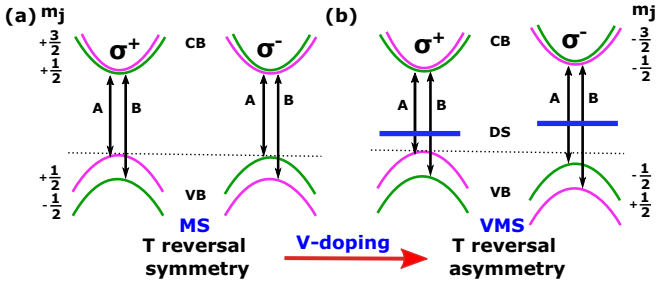

FIG. 5. Schematic diagrams of the MS and VMS energy band structures. (a) MS with spin-orbit interaction and (b) VMS with spin-orbit interaction. According to the optical selection rule, the Δm_j value [4] should be $+1$ for a σ^+ transition and -1 for a σ^- transition. The additional energy shift in K′ is induced by V doping. Magenta and green represent spin-up and spin-down states in valleys. CB, conduction band; DS, doped states; VB, valence band.

of valley polarization is described in Fig. 5. In pristine MS, because of the spin-orbit interaction, the spin splitting occurs at two different valleys with an opposite sign, as shown in Fig. 5(a). After doping, the valley degeneracy is lifted up and new doped states are formed near the valence band, because of which valley polarization couples with spin polarization, as shown in Fig. 5(b). The valley polarization can be controlled by controlling the concentration of the vanadium dopant.

IV. CONCLUSION

In conclusion, substitutional vanadium doping in an MoS_2 monolayer lattice is shown here, and the resulting VMS monolayers are shown to exhibit room-temperature valley polarization and valley splitting of ∼35 meV. The valley splitting is confirmed by two different experiments: first, with conventional chirality-selective emission/excitation-based PL measurements and second with SHEL-based reflection measurements. The PL measurements show that the valley polarization in VMS is much higher (∼42%) in comparison to that in MS (<12%). The SHEL measurements indicate the difference in the centroid position of σ^+ and σ^- in MS and VMS, along with a drastic change in the slope of the SHEL curve. The reduced shift of circularly polarized components in VMS in comparison to that of MS (or SiO_2) signifies an increase in the ellipticity of the reflected light. These changes in the SHEL on VMS is due to the difference in the reflected intensity of the two circular components causing an ellipticity in the reflected beam. This can be due to the modifications in the electronic band structure of VMS, as shown by the DFT-based calculations. Hence, the study paves possibilities of developing engineered, MoS_2-based atomically thin opto-spintronic devices, and establishing SHEL-based weak value enhancement as a promising tool for studying the valley physics of materials.

ACKNOWLEDGMENTS

Authors from Tata Institute of Fundamental Research appreciate the support of the Department of Atomic Energy, Government of India (Project Identification No. RTI 4007). T.N.N. and G.R. acknowledge the financial support from DST-SERB, Government of India SUPRA scheme (Grant No. SPR/2020/000220). The TEM and XPS studies were performed in the Laboratorio de Microscopias Avanzadas (LMA), Universidad de Zaragoza, Spain. The authors thank G. Antorrena (LMA) for the XPS measurements. R.A. acknowledges support from Spanish MICINN (Grant No. PID2019-104739GB-100/AEI/10.13039/501100011033), the Government of Aragon (projects DGA E13-20R; FEDER, EU), and from the European Union H2020 programs "ESTEEM3" (Grant No. 823717) and Graphene Flagship (Grant No. 881603).

[1] D. Xiao, G.- B. Liu, W. Feng, X. Xu, and W. Yao, Coupled Spin and Valley Physics in Monolayers of MoS_2 and Other Group-VI Dichalcogenides, Phys. Rev. Lett. **108**, 196802 (2012).

[2] Z. Y. Zhu, Y. C. Cheng, and U. Schwingenschlögl, Giant spin-orbit-induced spin splitting in two-dimensional transition-metal dichalcogenide semiconductors, Phys. Rev. B **84**, 153402 (2011).

[3] S. A. Vitale, D. Nezich, J. O. Varghese, P. Kim, N. Gedik, P. Jarillo-Herrero, D. Xiao, and M. Rothschild, Valleytronics: Opportunities, challenges, and paths forward, Small **14**, 1801483 (2018).

[4] K. F. Mak, K. He, J. Shan, and T. F. Heinz, Control of valley polarization in monolayer MoS_2 by optical helicity, Nat. Nanotechnol. **7**, 494 (2012).

[5] H. Zeng, J. Dai, W. Yao, D. Xiao, and X. Cui, Valley polarization in MoS_2 monolayers by optical pumping, Nat. Nanotechnol. **7**, 490 (2012).

[6] A. Srivastava, M. Sidler, A. V. Allain, D. S. Lembke, A. Kis, and A. Imamoğlu, Valley Zeeman effect in elementary optical excitations of monolayer WSe_2, Nat. Phys. **11**, 141 (2015).

[7] Z. Zhu, A. Collaudin, B. Fauqué, W. Kang, and K. Behnia, Field-induced polarization of Dirac valleys in bismuth, Nat. Phys. **8**, 89 (2012).

[8] D. Gunlycke and C. T. White, Graphene Valley Filter Using a Line Defect, Phys. Rev. Lett. **106**, 136806 (2011).

[9] O. Gunawan, Y. P. Shkolnikov, K. Vakili, T. Gokmen, E. P. De Poortere, and M. Shayegan, Valley Susceptibility of an Interacting Two-Dimensional Electron System, Phys. Rev. Lett. **97**, 186404 (2006).

[10] H.- Z. Lu, W. Yao, D. Xiao, and S.- Q. Shen, Intervalley Scattering and Localization Behaviors of Spin-Valley Coupled Dirac Fermions, Phys. Rev. Lett. **110**, 016806 (2013).

[11] O. L. Sanchez, D. Ovchinnikov, S. Misra, A. Allain, and A. Kis, Valley polarization by spin injection in a light-emitting van der Waals heterojunction, Nano Lett. **16**, 5792 (2016).

[12] Y. Li, J. Ludwig, T. Low, A. Chernikov, X. Cui, G. Arefe, Y. D. Kim, A. M. Van Der Zande, A. Rigosi, and H. M. Hill, Valley Splitting and Polarization by the Zeeman Effect in Monolayer $MoSe_2$, Phys. Rev. Lett. **113**, 266804 (2014).

[13] G. Aivazian, Z. Gong, A. M. Jones, R.- L. Chu, J. Yan, D. G. Mandrus, C. Zhang, D. Cobden, W. Yao, and X. Xu, Magnetic

control of valley pseudospin in monolayer WSe_2, Nat. Phys. **11**, 148 (2015).

[14] D. MacNeill, C. Heikes, K. F. Mak, Z. Anderson, A. Kormányos, V. Zólyomi, J. Park, and D. C. Ralph, Breaking of Valley Degeneracy by Magnetic Field in Monolayer $MoSe_2$, Phys. Rev. Lett. **114**, 037401 (2015).

[15] T. Cao, G. Wang, W. Han, H. Ye, C. Zhu, J. Shi, Q. Niu, P. Tan, E. Wang, and B. Liu, Valley-selective circular dichroism of monolayer molybdenum disulphide, Nat. Commun. **3**, 1 (2012).

[16] T. Norden, C. Zhao, P. Zhang, R. Sabirianov, A. Petrou, and H. Zeng, Giant valley splitting in monolayer WS_2 by magnetic proximity effect, Nat. Commun. **10**, 4163 (2019).

[17] K. L. Seyler, D. Zhong, B. Huang, X. Linpeng, N. P. Wilson, T. Taniguchi, K. Watanabe, W. Yao, D. Xiao, M. A. McGuire, K. M. C. Fu, and X. Xu, Valley manipulation by optically tuning the magnetic proximity effect in WSe_2/CrI_3 heterostructures, Nano Lett. **18**, 3823 (2018).

[18] C. Zhao, T. Norden, P. Zhang, P. Zhao, Y. Cheng, F. Sun, J. P. Parry, P. Taheri, J. Wang, and Y. Yang, Enhanced valley splitting in monolayer WSe_2 due to magnetic exchange field, Nat. Nanotechnol. **12**, 757 (2017).

[19] N. Singh and U. Schwingenschlögl, A route to permanent valley polarization in monolayer MoS_2, Adv. Mater. **29**, 2 (2017).

[20] Y. C. Cheng, Q. Y. Zhang, and U. Schwingenschlögl, Valley polarization in magnetically doped single-layer transition-metal dichalcogenides, Phys. Rev. B **89**, 155429 (2014).

[21] Q. Li, X. Zhao, L. Deng, Z. Shi, S. Liu, Q. Wei, L. Zhang, Y. Cheng, L. Zhang, H. Lu, W. Gao, W. Huang, C. W. Qiu, G. Xiang, S. J. Pennycook, Q. Xiong, K. P. Loh, and B. Peng, Enhanced valley Zeeman splitting in Fe-doped monolayer MoS_2, ACS Nano **14**, 4636 (2020).

[22] L.- A. T. Nguyen, K. P. Dhakal, Y. Lee, W. Choi, T. D. Nguyen, C. Hong, D. H. Luong, Y.- M. Kim, J. Kim, and M. Lee, Spin-selective hole–exciton coupling in a V-doped WSe_2 ferromagnetic semiconductor at room temperature, ACS Nano **15**, 20267 (2021).

[23] K. R. Sahoo, T. P. Chakravarthy, R. Sharma, S. Bawari, S. Mundlia, S. Sasmal, K. V. Raman, T. N. Narayanan, and N. K. Viswanathan, Probing proximity-tailored high spin-orbit coupling in 2D materials, Adv. Quantum Technol. **3**, 2000042 (2020).

[24] O. Hosten and P. Kwiat, Observation of the spin Hall effect of light via weak measurements, Science **319**, 787 (2008).

[25] K. Y. Bliokh and A. Aiello, Goos–Hänchen and Imbert–Fedorov beam shifts: An overview, J. Opt. **15**, 14001 (2013).

[26] J. J. Panda, K. R. Sahoo, A. Praturi, A. Lal, N. K. Viswanathan, T. N. Narayanan, and G. Rajalakshmi, High-Sensitivity Characterization of Ultra-Thin Atomic Layers Using Spin-Hall Effect of Light, J. Appl. Phys. **132**, 075302 (2022).

[27] Q. Zhang, J. Li, and X. Liu, Optical lateral forces and torques induced by chiral surface-plasmon-polaritons and their potential applications in recognition and separation of chiral enantiomers, Phys. Chem. Chem. Phys. **21**, 1308 (2019).

[28] X. Yu, X. Wang, Z. Li, L. Zhao, F. Zhou, J. Qu, and J. Song, Spin Hall effect of light based on a surface plasmonic platform, Nanophotonics **10**, 3031 (2021).

[29] See Supplemental Material at http://link.aps.org/supplemental/10.1103/PhysRevMaterials.6.085202 for more detailed information regarding growth, properties, DFT-based calculations, growth schematics, structural characterizations, SEM, SEM-EDX, PL, the circular polarized setup, a SHEL schematic, a SHEL-based valley study, and a projected density of states plot from DFT analysis.

[30] R. Sharma, K. R. Sahoo, P. K. Rastogi, R. K. Biroju, W. Theis, and T. N. Narayanan, On the synthesis of morphology-controlled transition metal dichalcogenides via chemical vapor deposition for electrochemical hydrogen generation, Phys. Status Solidi Rapid Res. Lett. **13**, 1900257 (2019).

[31] J. Zou, Z. Cai, Y. Lai, J. Tan, R. Zhang, S. Feng, G. Wang, J. Lin, B. Liu, and H.-M. Cheng, Doping concentration modulation in vanadium-doped monolayer molybdenum disulfide for synaptic transistors, ACS Nano **15**, 7340 (2021).

[32] J. Zhou *et al.*, A library of atomically thin metal chalcogenides, Nature (London) **556**, 355 (2018).

[33] L. Zhang, G. Wang, Y. Zhang, Z. Cao, Y. Wang, T. Cao, C. Wang, B. Cheng, W. Zhang, and X. Wan, Tuning electrical conductance in bilayer MoS_2 through defect-mediated interlayer chemical bonding, ACS Nano **14**, 10265 (2020).

[34] S. Mignuzzi, A. J. Pollard, N. Bonini, B. Brennan, I. S. Gilmore, M. A. Pimenta, D. Richards, and D. Roy, Effect of disorder on Raman scattering of single-layer MoS_2, Phys. Rev. B **91**, 195411 (2015).

[35] B. Peng, G. Yu, Y. Zhao, Q. Xu, G. Xing, X. Liu, D. Fu, B. Liu, J. R. S. Tan, and W. Tang, Achieving ultrafast hole transfer at the monolayer MoS_2 and CH_3NH_3PbI perovskite interface by defect engineering, ACS Nano **10**, 6383 (2016).

[36] T. Zhang, K. Fujisawa, F. Zhang, M. Liu, M. C. Lucking, R. N. Gontijo, Y. Lei, H. Liu, K. Crust, and T. Granzier-Nakajima, Universal in situ substitutional doping of transition metal dichalcogenides by liquid-phase precursor-assisted synthesis, ACS Nano **14**, 4326 (2020).

[37] L. Liu, U. Diaz, R. Arenal, G. Agostini, P. Concepcion, and A. Corma, Generation of subnanometric platinum with high stability during transformation of a 2D zeolite into 3D, Nat. Mater. **16**, 132 (2017).

[38] F. L. Deepak, A. Mayoral, and R. Arenal, *Advanced Transmission Electron Microscopy: Applications to Nanomaterials* (Springer, Cham, 2015).

[39] M. Pelaez-Fernandez, Y.- C. Lin, K. Suenaga, and R. Arenal, Optoelectronic properties of atomically thin $Mo_xW_{(1-x)}S_2$ nanoflakes probed by spatially-resolved monochromated EELS, Nanomaterials **11**, 3218 (2021).

[40] S. Hofmann, *Auger- and X-ray Photoelectron Spectroscopy in Materials Science: A User-Oriented Guide* (Springer Science & Business Media, Berlin, 2012), Vol. 49.

[41] P. K. Nayak, F.- C. Lin, C.- H. Yeh, J.- S. Huang, and P.- W. Chiu, Robust room temperature valley polarization in monolayer and bilayer WS_2, Nanoscale **8**, 6035 (2016).

[42] B. Zhu, H. Zeng, J. Dai, Z. Gong, and X. Cui, Anomalously robust valley polarization and valley coherence in bilayer WS_2, Proc. Natl. Acad. Sci. USA **111**, 11606 (2014).